Biochemistry **2007,** *46,* 8569−8578

Characterization of the Nitrosyl Adduct of Substrate-Bound Mouse Cysteine Dioxygenase by Electron Paramagnetic Resonance: Electronic Structure of the Active Site and Mechanistic Implications[†]

Brad S. Pierce,*[,‡] Jessica D. Gardner,[§] Lucas J. Bailey,[‡] Thomas C. Brunold,[§] and Brian G. Fox[‡]

Department of Biochemistry, University of Wisconsin, 433 Babcock Drive, Madison, Wisconsin 53706, and Department of Chemistry, University of Wisconsin, 1101 University Avenue, Madison, Wisconsin 53706

Received April 9, 2007; Revised Manuscript Received May 16, 2007

ABSTRACT: Mammalian cysteine dioxygenase (CDO) is a non-heme iron metalloenzyme that catalyzes the first committed step in oxidative cysteine catabolism. The active site coordination of CDO comprises a mononuclear iron ligated by the Nϵ atoms of three protein-derived histidines, thus representing a new variant on the 2-histidine-1-carboxylate (2H1C) facial triad motif. Nitric oxide was used as a spectroscopic probe in investigating the order of substrate−O_2 binding by EPR spectroscopy. In these experiments, CDO exhibits an ordered binding of L-cysteine prior to NO (and presumably O_2) similar to that observed for the 2H1C class of non-heme iron enzymes. Moreover, the CDO active site is essentially unreactive toward NO in the absence of substrate, suggesting an obligate ordered binding of L-cysteine prior to NO. Typically, addition of NO to a mononuclear non-heme iron center results in the formation of an $\{FeNO\}^7$ ($S = {}^3/_2$) species characterized by an axial EPR spectrum with g_x, g_y, and g_z values of ~4, ~4, and ~2, respectively. However, upon addition of NO to CDO in the presence of substrate L-cysteine, a low-spin $\{FeNO\}^7$ ($S = {}^1/_2$) signal that accounts for ~85% of the iron within the enzyme develops. Similar $\{FeNO\}^7$ ($S = {}^1/_2$) EPR signals have been observed for a variety of octahedral mononuclear iron−nitrosyl synthetic complexes; however, this type of iron−nitrosyl species is not commonly observed for non-heme iron enzymes. Substitution of L-cysteine with isosteric substrate analogues cysteamine, 3-mercaptopropionic acid, and propane thiol did not produce any analogous $\{FeNO\}^7$ signals ($S = {}^1/_2$ or ${}^3/_2$), thus reflecting the high substrate specificity of the enzyme observed by a number of researchers. The unusual $\{FeNO\}^7$ ($S = {}^1/_2$) electronic configuration adopted by the substrate-bound iron−nitrosyl CDO (termed $\{ES\text{-}NO\}^7$) is a result of the bidentate thiol/amine coordination of L-cysteine in the NO-bound CDO active site. DFT computations were performed to further characterize this species. The DFT-predicted geometric parameters for $\{ES\text{-}NO\}^7$ are in good agreement with the crystallographically determined substrate-bound active site configuration of CDO and are consistent with known iron−nitrosyl model complexes. Moreover, the computed EPR parameters (g and A values) are in excellent agreement with experimental results for this CDO species and those obtained from comparable synthetic $\{FeNO\}^7$ ($S = {}^1/_2$) iron−nitrosyl complexes.

In mammals, the first step in oxidative cysteine catabolism is catalyzed by the non-heme iron enzyme cysteine dioxygenase (CDO)[1] (*1*−*4*). The product of the CDO-catalyzed reaction is cysteinesulfinic acid, which is the precursor in hypotaurine and taurine biosynthesis (*5*−*8*). The function of this enzyme is of considerable medical interest because imbalances in cysteine catabolism have been implicated in a variety of neurological disorders (motor neuron disease, Parkinson's, and Alzheimer's) as well as autoimmune diseases (rheumatoid arthritis and systemic lupus erythematosus) (*5*, *9*, *10*). Furthermore, increased levels of L-cysteine produce excitotoxic effects on the mammalian brain (*11*, *12*).

CDO incorporates both oxygen atoms from O_2 into the product without an external reductant; hence, CDO is classified as a dioxygenase (*4*). CDO also exhibits high specificity for L-cysteine, showing little or no reactivity with D-cysteine, glutathione, L-cystine, or cysteamine (*1*−*4*). Although results from steady-state kinetic studies of recombinant rat CDO are available, few direct mechanistic details of the chemical reaction have been elucidated (*5*, *8*, *13*).

Recently, multiple high-resolution crystal structures of mammalian CDO have been determined [Protein Data Bank (PDB) entries 2ATF, 2B5H, and 2IC1], revealing an active site comprising a mononuclear iron ligated by the Nϵ atoms of His86, His88, and His140, representing a new facial triad

---

[†] This work was supported by NIH Grant 1 F32 GM074385 to B.S.P., NIH Grant GM50583 and NSF Grant MCB-0316232 to B.G.F., and NIH Grant GM64631 to T.C.B.

* To whom correspondence should be addressed: Department of Biochemistry, University of Wisconsin, 433 Babcock Dr., Madison, WI 53706. Phone: (608) 262-0254, ext. 2107. Fax: (608) 262-3453. E-mail: bpierce@biochemistry.wisc.edu.

[‡] Department of Biochemistry.

[§] Department of Chemistry.

[1] Abbreviations: CDO, cysteine dioxygenase; EPR, electron paramagnetic resonance; DFT, density functional theory; TCEP, tris(2-carboxyethyl)phosphine hydrochloride; EDTA, ethylenediaminetetraacetic acid; 2H1C, 2-histidine-1-carboxylate.

10.1021/bi700662d CCC: $37.00

Scheme 1

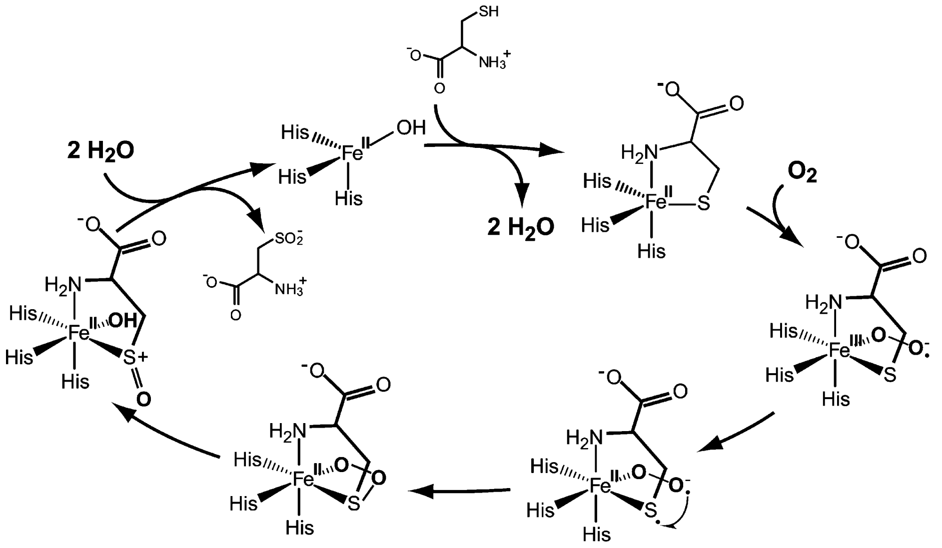

variant (*14*−*16*). While uncommon, deviations from the 2-His-1-carboxylate (2H1C) motif are observed in other members of the cupin family of protein folds (*17*). CDO also contains a covalently cross-linked cysteine−tyrosine adduct (C93−Y157) within 3.3 Å of the iron active site (*14*−*16*). An analogous post-transcriptional modification has been observed in the copper-radical enzyme galactose oxidase (*18*−*21*). On the basis of this similarity and the proximity of the C93−Y157 adduct to the active site, a tyrosine radical has been proposed to be involved in catalysis (*15*). However, there is currently no direct evidence of the role of this covalent modification in CDO.

Within the 2H1C family of non-heme diiron enzymes, a general mechanism for catalysis based on extensive mechanistic, spectroscopic, and crystallographic characterization has emerged (*22*−*24*). Typically, the monoanionic 2H1C active site contains a six-coordinate ferrous iron with solvent molecules serving as the non-protein ligands. Moreover, the reduced active site is mostly unreactive toward O_2 until substrate and cofactor are bound (*24*). Thus, activation of O_2 occurs only following the ordered binding of substrate and/or cofactor. The subsequent mechanism following reductive activation of O_2 is specific for each of the five classes of 2H1C enzymes (*25*). On the basis of this model and the limited mechanistic information that is available, the reaction mechanism shown in Scheme 1 was proposed for CDO in which L-cysteine adopts bidentate coordination to the ferrous site through a thiolate and an amino group (*14*). This exact bidentate coordination was recently confirmed by cocrystallization of the enzyme in the presence of substrate (*15*). Following substrate ligation, O_2 has been proposed to bind to the remaining metal coordination site and become activated to produce a Fe^{III}−superoxo ternary complex with radical character at the cysteine sulfur.

The work presented here utilizes EPR spectroscopy and DFT computational methods in probing several aspects of the proposed CDO catalytic cycle: (1) the resting oxidation state of the enzyme, (2) the order of binding for L-cysteine and O_2 by the use of nitric oxide (NO) as a spectroscopic probe (*26*, *27*), (3) the degree of substrate specificity, and (4) the electronic structure of the substrate-bound iron−nitrosyl CDO active site. On the basis of these results, a model for the substrate-bound CDO active site is proposed and discussed in light of the known spectroscopic, structural, and enzymatic properties of the enzyme.

MATERIALS AND METHODS

Protein Purification. Overexpression and purification of the recombinant CDO enzyme were carried out with minor modifications as described previously by McCoy et al. (*14*). In a typical purification, ~50 g of *Escherichia coli* BL21-(DE3) cell paste was thawed in 25 mM MOPS buffer (pH 7). This slurry was then treated with DNase, RNase, and lysozyme for 20 min prior to pulse sonication for 5 min. After sonication, the suspension was centrifuged for 1 h at 40000*g* and 4 °C. The supernatant was decanted from the pellet, diluted with the same buffer 1:1, and loaded onto a DEAE-Sepharose anion exchange column [5 cm (diameter, D) × 11.5 cm (length, L)] pre-equilibrated in MOPS buffer. The anion exchange column was washed with 1 column volume of buffer prior to gradient elution from 50 to 300 mM NaCl. The fractions were pooled on the basis of the presence of the maltose binding protein−CDO fusion (MBP−CDO, $M_r \sim 60$ kDa), observed by SDS−PAGE, and concentrated using an Amicon stir cell equipped with an YM-30 ultrafiltration membrane. Tobacco etch virus (TEV) protease was used to release CDO from the fusion protein in 50 mM MOPS, 100 mM NaCl, and 0.3 mM tris(2-carboxyethyl)phosphine hydrochloride (pH 7.5) overnight at 4 °C. Confirmation of full cleavage was accomplished by SDS−PAGE, which showed two protein bands at ~20 and 40 kDa for CDO and MBP, respectively. The MBP was separated from CDO using Sephacryl S-100 (5 cm D × 80 cm L) size exclusion chromatography in 25 mM MOPS, 50 mM maltose, and 150 mM NaCl (pH 7). Addition of maltose was necessary for resolving MBP from CDO. All attempts to separate these two proteins by either anion exchange or size exclusion chromatography in the absence of maltose were unsuccessful. As before, the fractions of purified CDO were pooled on the basis of the presence of CDO as determined by SDS−PAGE and concentrated. The purified CDO enzyme was assayed for iron content and specific activity as described previously (*13*, *14*). The protein concentration was determined by a Bradford assay. Iron-reconstituted CDO was prepared by addition of a 1 mM [Fe(NH_4)$_2$(SO_4)$_2$], 10 mM ascorbic acid, 25 mM MOPS solution (pH 7) at a 5-fold excess relative to protein concentration.

Iron Analysis. The colorimetric determination of iron content by bathophenanthrolinedisulfonic acid was adapted from several published protocols (*28*, *29*). For the total iron assay, 100 μL of approximately 100 μM CDO was added to a microfuge tube. The protein solution was acid-hydrolyzed by addition of 50 μL of concentrated sulfuric acid. The resulting suspension was heated to 95 °C for 15 min. After digestion of the sample, 1.0 mL of 3 M acetate buffer (pH 7.5), 0.2 mL of 1% NH_2OH, and 0.2 mL of 0.3% bathophenanthrolinedisulfonic acid were added to the sample. The resulting solution (pH 4.5) was allowed to equilibrate for 30 min at ambient temperature to ensure complete reduction of all ferric iron to the ferrous state. Ferrous iron was assayed separately following the procedure described above in the absence of NH_2OH. Iron quantitation was performed spectrophotometrically ($\lambda = 535$ nm; $\epsilon = 22.1$ mM^{-1} cm^{-1}) (*28*, *29*). The difference between results obtained from the total iron and ferrous iron analyses was an indication of the remaining ferric iron within the sample. Results of the colorimetric assay were verified by quantitative EPR analysis of acid-hydrolyzed samples.

CDO Activity Assay. The rate of cysteinesulfinic acid formation was determined by HPLC as previously described (*14*). In a typical assay 1 μM CDO enzyme was allowed to react aerobically with L- or D-cysteine for up to 2 h at 37 °C in 20 mM ammonium acetate (pH 6.1). Samples were taken every 15 min up to 1 h for the determination of the quantities of L- or D-cysteine and cysteinesulfinic acid present in the reaction mixture by reverse-phase HPLC using 20 mM sodium acetate, 0.6% methanol, and 0.3% heptofluorobutyric acid (pH 5.0) as the mobile phase. Each sample aliquot was filtered by 0.22 μM centrifuge tube filtration (Corning, Spin-x) prior to analysis via HPLC. Injections (20 μL) were eluted at a flow rate of 1.0 mL/min on a Microsorb-MV 100 Å C18 column and detected at 218 nm. HPLC samples were analyzed using a Shimadzu LC-10AT instrument with an SPD-M10A diode array detector. Experiments involving hydroxyurea were performed under the same conditions with a 1000-fold excess of the free radical scavenger (1 mM hydroxyurea) relative to the enzyme concentration.

Preparation of Nitric Oxide Solutions. Nitric oxide is poisonous, and therefore, extreme caution should be employed in its use. Nitric oxide gas (Matheson, 99% pure) was sparged through an aqueous 5 M solution of NaOH to remove trace impurities from the cylinder. Following the NaOH treatment, the nitric oxide gas was passed through an Ascarite II (Sigma-Aldrich catalog no. 223913) column so the higher nitrogen oxides could be removed. All NO additions were performed by titrating a NO-saturated 25 mM MOPS buffer (pH 7) into protein samples via a Hamilton gastight syringe. The concentration of NO within the 25 mM MOPS buffer (pH 7) was measured by titration into a standard solution of 1.0 mM [Fe(NH_4)$_2$(SO_4)$_2$] and 10 mM EDTA, in 0.2 M acetate, at pH 5 and 4 °C. All EPR samples of CDO were rigorously degassed on a Schlenk line prior to the addition of nitric oxide. Unless otherwise noted, all additions of NO were stoichiometric with ferrous iron.

EPR Spectroscopy. X-Band (9.25 GHz) EPR spectra were recorded on a Bruker ESP 300E spectrometer equipped with an Oxford ITC4 cryostat for low-temperature measurements. The microwave frequency and magnetic field were calibrated by using a Hewlett-Packard model 5340 frequency counter and a NMR gaussmeter, respectively. A modulation frequency of 100 kHz was used for all EPR spectra. All experimental data were collected under nonsaturating conditions.

EPR Simulations. Analysis of the EPR spectra utilized the general spin Hamiltonian

$$\mathbf{H}_s = D\left(S_z^{\,2} - \frac{S^2}{3}\right) + E(S_x^{\,2} - S_y^{\,2}) + \beta\mathbf{B}\cdot\mathbf{g}\cdot\mathbf{S} + \mathbf{S}\cdot\mathbf{A}\cdot\mathbf{I}$$

where D and E are the axial and rhombic zero-field splitting (zfs) parameters, respectively, and $\mathbf{g}$ is the g tensor (*30*). Nuclear hyperfine interactions (**A**) were treated with second-order perturbation theory. Simulations of the EPR spectra are calculated from diagonalization of the general spin Hamiltonian using Spin Count version 2.2.7 created by Professor M. P. Hendrich at Carnegie Mellon University (Pittsburgh, PA). This program computes the powder pattern for a uniform spherical distribution of the magnetic field vector **B**, and the transition intensities are calculated using “Fermi’s golden rule”. Least-squares and deconvolution analysis of the spectra are combined to allow relevant parameters to vary while maintaining a sum of multiple species that best fits the experimental data. The simulations are generated with consideration of all intensity factors, both theoretical and experimental, to allow determination of concentrations for species (*31*). This allows for quantitative concentration determination for an experimental spectrum via comparison of the signal intensity to the simulated spectrum. The only unknown factor relating the spin concentration to signal intensity is an instrumental factor that depends on the microwave detection system. However, this factor is determined using a Cu(II)EDTA spin standard. The observed line width for the $S = {}^1/_2$ signal is dominated by g strain and can be fit using Gaussian distributions in g values, termed $\sigma g_{x,y,z}$.

DFT Calculations. Active site models for the CDO species with NO and cysteine bound to the Fe^{II} ion were generated by density functional theory (DFT) geometry optimizations using the Amsterdam Density Functional (ADF) 2006.01 software package (*32*−*35*). The calculations employed ADF basis set IV (triple-ζ with single polarization), an integration constant of 4.0, the Vosko−Wilk−Nusair local density approximation (*36*), and the nonlocal gradient corrections of Becke (*37*) and Perdew (*38*). Core orbitals were frozen through 1s (O, N, C) or 2p (Fe, S). Initial structures were derived from published X-ray crystallographic data for native and cysteine-bound CDO (*14*, *15*, *39*). The models included the three first-sphere His residues ligated to a low-spin Fe^{II} ion, as well as a bidentate cysteine ligand with S and N coordination, and NO as a the sixth ligand. The His residues were modeled as 4-ethylimidazole, and the terminal methyl groups were held frozen during the optimization. The positions of all other atoms were allowed to vary.

Spin-unrestricted single-point DFT calculations were performed on the optimized structures using the ORCA 2.4 software package (*40*) developed by F. Neese. The computations utilized Becke’s three-parameter hybrid exchange functional (*41*) with the Lee−Yang−Parr correlation functional (*42*) (B3LYP), as well as a combination of three different basis sets: (i) the "core-properties" basis set (*43*) with extended polarization (*44*) [CP(PPP)] for Fe, (ii) Kutzelnigg's basis set for NMR and EPR parameters (*45*) (IGLO-III) for the N atom of the NO ligand, and (iii) Ahlrichs' triple-ζ valence basis set (*46*) with one set of polarization functions [TZV(P)] for the remaining non-hydrogen atoms in conjunction with the corresponding auxiliary basis set (TZV/J) (*47*, *48*). gOpenMol (*49*, *50*) developed by Laaksonen was used to generate isosurface plots of molecular orbitals using an isodensity value of 0.03 au.

EPR parameters were computed with ORCA by solving the coupled-perturbed SCF (CP-SCF) equations (*51*, *52*) using the B3LYP hybrid functional and the basis sets described above. These calculations included all orbitals within a ±100 hartree window around the HOMO−LUMO gap, with the origin of the **g** tensor defined as the center of electronic charge. A high-resolution radial grid with an integration accuracy of 7.0 was used for the Fe atom and the N atom of the NO ligand.

RESULTS

Iron Analysis. The concentrations of total and ferrous iron were determined by optical spectroscopy using the procedure outlined in Materials and Methods. Briefly, samples of purified CDO were acid-denatured in the presence of the strong ferrous iron chelator bathophenanthrolinedisulfonic acid. The total iron content was determined by UV−visible spectroscopy in the presence of excess hydroxylamine using the published extinction coefficient for the ferrous−bathophenanthroline complex ($\epsilon_{535} = 22.1$ mM^{-1} cm^{-1}) (*28*, *29*). Alternatively, the amount of ferrous iron was determined in the absence of reductant. In multiple preparations of CDO, nearly all (∼99%) of the iron was found to be in the ferrous state as determined by UV−visible spectroscopy. Furthermore, in the absence of any external reductant, only trace levels of ferric iron (<5% of the total) were observed by EPR spectroscopy. Therefore, the active site of resting CDO stabilizes ferrous iron under aerobic conditions. This observation supports the initial step of the mechanism shown in Scheme 1 and is consistent with the established mechanism of enzymes containing the classic 2H1C active site motif (note, however, that in multiple enzyme preparations the ferrous iron content was typically only ∼50% of the total protein concentration).

Steady-State Enzyme Kinetics. CDO was prepared and assayed for activity according to the published reverse-phase HPLC method (*13*, *14*). The Michaelis−Menten constant (K_m) and k_{cat} were measured for isolated CDO as 6.5 mM and 0.8 s^{-1} ($k_{cat}/K_m = 0.12$ mM/s), respectively. As previously mentioned, the ferrous iron content of purified CDO suggested ∼50% iron incorporation. However, upon ferrous iron reconstitution, the resulting steady-state kinetic parameters for CDO exhibited a 2-fold increase in k_{cat} (1.6 s^{-1}) with no significant effect on the Michaelis constant (K_m = 5.4 mM). The kinetic parameters observed for reconstituted CDO are in good agreement with published results for both the recombinant mouse and human CDO enzymes (*5*, *13*−*15*). Moreover, steady-state enzyme kinetics carried our here confirm the previous observation that CDO exhibits little activity toward the D-stereoisomer of cysteine (k_{cat}^{D}/k_{cat}^{L} < 7%) (*1*−*4*).

On the basis of the structural similarity between the covalently cross-linked C93−Y157 adduct observed in CDO and an analogous covalent modification observed within galactose oxidase (C228−Y272) (*20*, *21*), it has been proposed that the mechanism of CDO may also involve a tyrosine radical during catalysis (*15*). To test this hypothesis, the enzymatic activity of CDO was measured under saturating concentrations of L-cysteine in the presence of a known radical scavenger, hydroxyurea (*53*, *54*). In this experiment, no inhibition of the enzymatic activity of CDO was observed, even in the presence of a 1000-fold excess of hydroxyurea. Therefore, it is unlikely that any catalytically essential radicals are generated on the cross-linked C93−Tyr157 moiety during oxidative catabolism of L-cysteine.

NO Quantitation. The order in which L-cysteine and O_2 bind to CDO under turnover conditions was investigated by EPR spectroscopy using nitric oxide (NO) as a surrogate for O_2. Nitric oxide was added in stoichiometic amounts with respect to the iron content of purified CDO without iron reconstitution to minimize the amount of adventitious ferric iron in EPR samples. The concentration of NO within the saturated buffer was determined by titration into a standard solution of Fe^{II}-EDTA and 0.2 M sodium acetate (pH 5) at 4 °C via a Hamilton gastight syringe. Under these conditions, the binding of NO to Fe^{II}-EDTA was tight and well-defined (*55*, *56*). This permitted the amount of NO within the buffer to be determined via simulation of the axial EPR spectrum associated with the resulting $\{FeNO\}^7$ ($S = {}^3/_2$) Fe^{II}-EDTA-(NO) complex and comparison to a known Cu^{II}-EDTA standard. Using this procedure, the NO concentration was measured within the stock NO-saturated buffer as 2.9 ± 0.2 mM. At 4 °C, this value represents 96% of the published NO solubility in deionized water (*57*).

CDO NO Additions. As illustrated in Figure 1 (spectrum 1), addition of stoichiometric amounts of NO to anaerobic CDO in the absence of L-cysteine results in the formation of an axial $S = {}^3/_2$ EPR signal with the following effective g values: g_x, g_y, and $g_z \approx 4$, 4, and 2, respectively. The value for the axial zero-field splitting parameter (D) was determined by plotting the EPR signal intensity for this species versus $1/T$ and fitting the data to a Boltzman population distribution for a two-level system. This $\{FeNO\}^7$ ($S = {}^3/_2$) signal is spectroscopically indistinguishable from that of aqueous Fe^{II}-EDTA(NO) (*55*) with a D of 9 ± 1 cm^{-1} and an E/D of 0.001. The additional positive absorptive feature observed at $g = 1.98$ can be assigned to free NO in solution (*58*). However, in multiple preparations, the concentration of the $\{FeNO\}^7$ ($S = {}^3/_2$) species determined by quantitative simulation typically accounted for ≤15% (13 μM) of the total ferrous iron (100 μM) within the sample. Furthermore, increasing the amount of added NO up to a 5-fold excess relative to iron did not significantly alter the amount of $S = {}^3/_2$ $\{FeNO\}^7$ species observed. Addition of NO in excess of 5 equiv resulted in visible protein denaturation and aggregation. Aerobic addition of L-cysteine to this sample yielded a sharp EPR signal at $g = 4.3$ typical of high-spin Fe^{III} ($S = {}^5/_2$; $E/D \sim {}^1/_3$) with a concomitant loss of the $S = {}^3/_2$ signal. Thus, in the absence of substrate the ferrous active site of CDO appears to be inaccessible to, or unreactive toward, NO. Alternatively, as shown in Figure 1 (spectrum

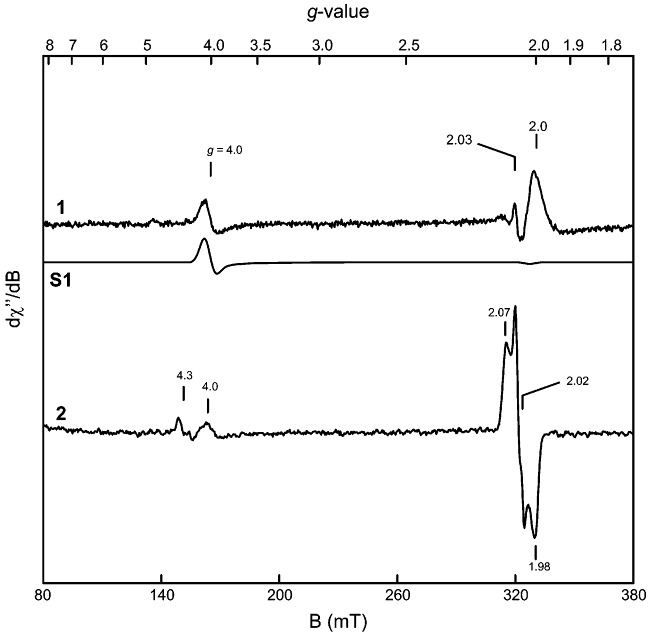

FIGURE 1: X-Band EPR spectra showing the ordered binding of NO to CDO and substrate-bound CDO. Spectrum 1: anaerobic addition of 4 molar equiv of NO to 100 μM CDO. The amount of $\{FeNO\}^7$ ($S = {}^3/_2$) species in spectrum 1 was determined by simulation (S1) to be 13 μM. Spectrum 2: stoichiometric addition of NO to 85 μM CDO precomplexed with L-cysteine. Instrumental parameters: microwave frequency, 9.25 GHz; modulation frequency, 100 kHz; modulation amplitude, 1.0 mT; temperature, 20 K; microwave power, 0.1 mW (−33 dB). Simulation parameters for $\{FeNO\}^7$ spectrum S1: $S = {}^3/_2$; $D = 9$ cm^{-1}; $E/D = 0.001$; g_x, g_y, and g_z = 2.0, 2.0, and 2.0, respectively; $\sigma_B = 2.7$ mT.

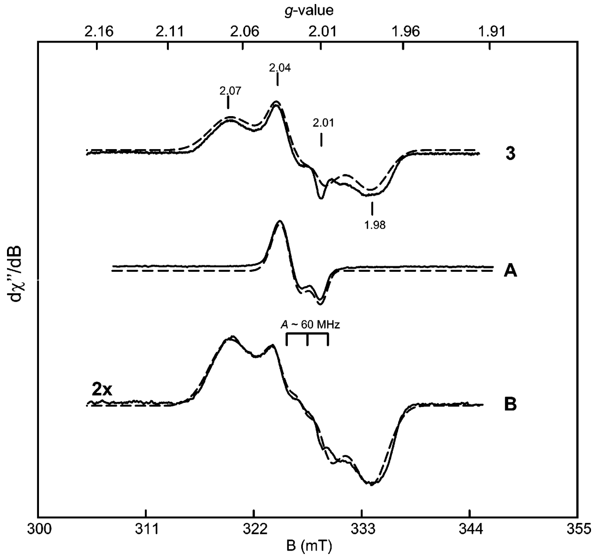

FIGURE 2: X-Band EPR spectra of substrate-bound iron−nitrosyl CDO. A quantitative component sum simulation for the spectra associated with species A and B was utilized to generate the simulation for spectrum 3. Using this technique, the respective concentration for each species was determined by least-squares analysis to be 4 and 57 μM, respectively. Sample conditions: CDO and L-cysteine concentrations for spectrum 3 of 85 and 900 μM, respectively. Instrumental parameters: microwave frequency, 9.25 GHz; modulation frequency, 100 kHz; modulation amplitude, 0.63 mT; temperature, 20 K; microwave power, 0.01 mW (−43 dB). Simulation parameters for spectrum A: $S = {}^1/_2$; g_x, g_y, and g_z = 2.03, 2.03, and 2.01, respectively; σ_B = 0.4 mT. Simulation parameters for spectrum B: $S = {}^1/_2$; g_x, g_y, and g_z = 2.070, 2.022, and 1.979, respectively; (^{14}N; $I = 1$) A_x, A_y, and A_z = 27, 60, and 28 MHz, respectively; σg_x, σg_y, and σg_z = 0.0059, 0.0088, and 0.0003, respectively; σ_B = 0.4 mT.

2), when stoichiometric NO was added to a preformed complex of CDO and L-cysteine, a new signal developed in the EPR spectrum $g \approx 2$. As with the addition of NO in the absence of substrate, only a trace amount (5 μM) of the $\{FeNO\}^7$ ($S = {}^3/_2$) signal was observed. The sharp EPR signal at $g = 4.3$ is assigned to high-spin ferric iron and accounts for ~3 μM (<3% of the total iron).

The EPR spectrum shown in Figure 2 illustrates the $g = 2$ region of CDO precomplexed with L-cysteine prior to addition of NO. Spectrum 3 consists of two spectroscopically distinct $S = {}^1/_2$ signals (termed A and B). The individual contribution of each was determined by quantitative simulation and least-squares fitting. The sharp $S = {}^1/_2$ signal with g values of 2.04, 2.03, and 2.01 (spectrum A, solid line, Figure 2) was produced by addition of NO to a solution of L-cysteine and Fe^{II} in the absence of CDO. This spectrum arises from a known tetrahedral $[Fe(NO)_2(L)_2]$ complex commonly observed during NO additions (*59*−*62*). The quantitative simulation of spectrum A (dashed line) indicates an iron concentration of 4 μM (4.7% of the total iron). Since an identical A-type spectrum can be readily obtained in the absence of CDO, this signal is attributed to a contaminant. Alternatively, the appearance of spectrum B (solid line, Figure 2) is unique to the ordered combination of CDO, L-cysteine, and NO. Spectrum B exhibits greater g anisotropy than spectrum A, with observed g values of 2.07, 2.02, and 1.98. Additionally, spectrum B exhibited inhomogeneous saturation with a power at half-saturation ($P^{1/2}$) of 1.3 mW. Furthermore, the triplet hyperfine splitting (A_y = 60 MHz) at $g = 2.02$ is consistent with published values for a nitrogen ($I = 1$)-centered ^{14}NO radical (*63*, *64*). The A_x and A_z values exhibited by EPR spectrum B are significantly smaller than the central A_y splitting and thus cannot be completely resolved at this frequency. However, these features strongly contribute to the spectral line width in the g_x and g_z regions of the EPR spectra, and thus, an upper limit on the magnitude of A_x and A_y can be reasonably determined by simulation. The spin quantitation and simulation for spectrum B (dashed line) account for ~67% of the assayed ferrous iron in the sample (57 μM of 85 μM ferrous iron). However, titration of substrate-bound CDO with up to 1.5 equiv of NO showed ~85% formation of spectrum B relative to the total iron. Addition of more than 1.5 equiv of NO resulted in a decrease in the intensity of spectrum B and a complete disappearance for >4 equiv. The spectroscopic parameters used for the simulation of spectrum B are listed in Table 1. On the basis of these parameters, the species responsible for spectrum B is assigned as a substrate-bound iron−nitrosyl CDO species ($\{ES\text{-}NO\}^7$). A more complete description of this atypical $\{FeNO\}^7$ ($S = {}^1/_2$) species will be presented below.

To probe the substrate specificity of CDO, cysteamine, 3-mercaptopropionate, and 1-mercaptopropane were substituted for L-cysteine prior to the addition of NO. These substrate analogues are isosteric with the natural substrate but lack the carboxyl, amino, and both functional groups, respectively. Upon addition of NO, none of the substrate analogues yielded a B-type EPR spectrum analogous to that of $\{ES\text{-}NO\}^7$. Moreover, as with the addition of NO in the absence of L-cysteine, only trace levels of the more typical $\{FeNO\}^7$ ($S = {}^3/_2$) signal were observed. The complete lack

Table 1: Comparison between EPR Parameters for the $\{ES\text{-}NO\}^7$ ($S = {}^1/_2$) CDO Species Associated with Spectrum B and Synthetic $\{FeNO\}^7$ ($S = {}^1/_2$) Model Complexes

species	g_x	g_y	g_z	A_x (^{14}N)	A_y (^{14}N)	A_z (^{14}N)	ref
B	2.071	2.022	1.976	9.0×10^{-4} cm^{-1} (27 MHz)	20×10^{-4} cm^{-1} (60 MHz)	9.3×10^{-4} cm^{-1} (28 MHz)	this work
[L^{Pr}Fe(NO)]	2.07	2.02	1.99	$10(4) \times 10^{-4}$ cm^{-1} (30 MHz)	$21(2) \times 10^{-4}$ cm^{-1} (63 MHz)	$14(4) \times 10^{-4}$ cm^{-1} (42 MHz)	*64*
[Fe(NO)(cyclam-ac)]	2.056	2.012	1.968	$18(2) \times 10^{-4}$ cm^{-1} (54 MHz)	$21(1) \times 10^{-4}$ cm^{-1} (63 MHz)	$18(2) \times 10^{-4}$ cm^{-1} (54 MHz)	*67*
[Fe(NO)(cyclam-ac)]	2.042	2.022	1.977	$1(3) \times 10^{-4}$ cm^{-1} (3 MHz)	$25(1) \times 10^{-4}$ cm^{-1} (75 MHz)	$10(2) \times 10^{-4}$ cm^{-1} (30 MHz)	*67*

Table 2: Selected Bond Distances and Angles for DFT-Optimized Models 1 and 2 Compared to the Crystal Structure of Cysteine-Bound CDO in the Absence of NO (PDB entry 2IC1)

bond	model 1 (Å)	model 2 (Å)	2IC1 (Å)	bond angle	model 1 (deg)	model 2 (deg)	2IC1 (deg)
Fe−Nϵ(H86)	2.25	2.18	2.04	(H140)Nϵ−Fe−N(Cys)	166.9	177.9	171.6
Fe−Nϵ(H88)	2.12	2.24	2.07	(H86)Nϵ−Fe−Ne(H88)	84.9	87.6	96.8
Fe−ϵ(H140)	2.01	2.30	2.02	(H86)Nϵ−Fe−S(Cys)	90.4	88.8	124.9
Fe−S(Cys)	2.26	2.22	2.02	(H88)Nϵ−Fe−S(Cys)	175.3	172.5	128.9
Fe−S(Cys)	2.02	2.34	2.03	(Cys)N−Fe−S(Cys)	86.9	85.9	83.9
Fe−N(NO)	1.70	1.81	−	Fe−N−O(NO)	142.1	144.8	−
N−O(NO)	1.21	1.21	−	(H140)Nϵ−Fe−N(NO)	94.9	91.2	−

Table 3: Comparison between the Experimental EPR Parameters for the $\{ES\text{-}NO\}^7$ ($S = {}^1/_2$) CDO Species Associated with Spectrum B and the DFT-Computed Parameters for Models 1 and 2

DFT calculation	initial coordinates	resolution (Å)	g_x	g_y	g_z	A_x (^{14}N) (MHz)	A_y (^{14}N) (MHz)	A_z (^{14}N) (MHz)
1	2IC1	2.7	2.044	2.004	1.967	21	87	22
2	2ATF	1.75	2.064	2.032	1.983	2	71	18
B	−		2.071	2.022	1.976	27	60	28

of any $\{FeNO\}^7$ species generated upon addition of NO to CDO in the presence of these substrate analogues is consistent with the high substrate specificity previously reported for this enzyme (*1*−*4*). Furthermore, this result suggests that all functional groups (CO_2, SH, and NH_3) are required for coordination of substrate within the CDO active site. Alternatively, when D-cysteine was substituted for L-cysteine under the same conditions, an ∼40% yield of B was obtained as observed by EPR spectroscopy. Therefore, CDO exhibits only partial stereospecific preference for L-cysteine relative to the D-isomer upon formation of the $\{ES\text{-}NO\}^7$ complex. The high catalytic stereospecificity of CDO exhibited during steady-state catalysis can thus not be solely attributed to a difference in the binding constants between the two stereoisomers.

Electronic Structure Calculations. The $S = {}^1/_2$ spin state observed for $\{ES\text{-}NO\}^7$ is unusual in that iron−nitrosyl species typically exhibit an $S = {}^3/_2$ electronic ground state arising from the antiferromagnetic coupling of high-spin Fe^{III} ($S = {}^5/_2$) with NO^- ($S = 1$) (*55*, *63*, *64*). However, a similar $\{FeNO\}^7$ ($S = {}^1/_2$) electronic ground state was reported by Wieghardt and co-workers for two octahedral iron−nitrosyl model complexes with amine and thiolate coordination (*64*). Thus, the unusual low-spin configuration exhibited by $\{ES\text{-}NO\}^7$ is likely the result of the bidentate amine and thiolate coordination of L-cysteine to Fe^{II} (*15*). In fact, as shown in Table 1, one of these complexes (complex i) exhibits *g* and *A* values nearly identical to those of EPR spectrum B. Mössbauer and EPR spectroscopic characterization of these model complexes complemented with DFT calculations suggested that their unusual ground-state properties are consistent with a ligand-based $NO^\bullet$ radical ($S = {}^1/_2$) coordinated to a low-spin ($S = 0$) ferrous iron (*63*, *64*). To verify if the species associated with EPR spectrum B possesses a similar electronic structure, models of the $\{ES\text{-}NO\}^7$ active site were generated starting from two separate crystallographic data sets (PDB entries 2IC1 and 2ATF corresponding to calculation 1 and 2, respectively), and their geometric and EPR spectroscopic parameters were calculated using DFT methods. Table 2 compares the geometric parameters for both geometry-optimized models to those of the substrate-bound crystal structure (*15*). In the absence of NO (X-ray crystal structure, entry 2IC1 in Table 2), the substrate-bound active site exhibits nearly trigonal bipyramidal geometry with H86, H88, and the cysteine thiol group comprising the trigonal plane perpendicular to the (H140)Nϵ−Fe−N(cysteine) axis. In contrast, both DFT-optimized models exhibit a nearly octahedral geometry upon coordination of NO, with the major structural rearrangement involving an in-plane rotation of the coordinated cysteine thiol group toward H86 by ∼40°. Overall, both DFT models are in good agreement with each other, and the optimized atomic coordinates are within the resolution of the crystal structure. Furthermore, our models for the CDO $\{ES\text{-}NO\}^7$ complex are consistent with recent X-ray absorption spectroscopic data in that the average bond distance is larger for the enzyme−substrate complex (*65*). Moreover, the Fe−NO distances and Fe−N−O bond angles closely match those determined experimentally for similar iron−nitrosyl synthetic complexes (*63*, *64*, *66*).

To further validate DFT models 1 and 2 on the basis of experimental data, the *g* and *A* values were calculated by DFT using the B3LYP functional. As illustrated in Table 3, the EPR parameters calculated from both crystal structures agree well with the experimental values for the CDO $\{ES\text{-}NO\}^7$ complex. However, slightly better agreement was achieved with DFT model 2, which was based on the higher-resolution crystal structure. In particular, the large central

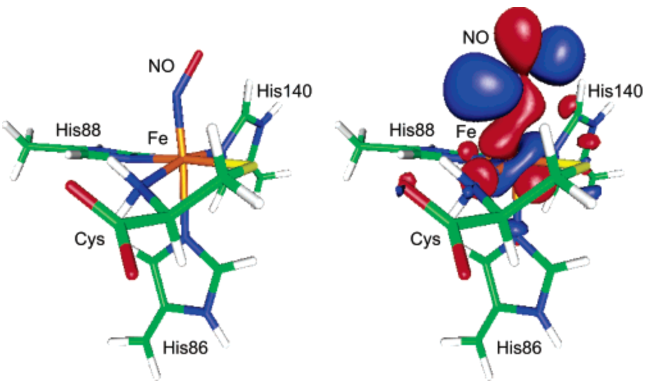

FIGURE 3: DFT-optimized structure (left) and isosurface plot of the singly occupied molecular orbital (right) of model 1 of the {ES-NO}^{7} CDO complex.

hyperfine splitting (A_y) predicted by both models is consistent with a ligand-centered (NO) radical (*64*, *67*). This agreement between experimental and calculated parameters suggests that our models provide an acceptable description of the NO- and L-cysteine-bound CDO species observed experimentally. Thus, these models can be used to gain additional insight into the electronic structure of this species. The molecular orbital (MO) description obtained from the DFT calculations on our optimized models is consistent with the assignment of the {ES-NO}^{7} complex as one containing a ligand-centered NO radical coordinated to a low-spin ferrous iron. The singly occupied molecular orbital (SOMO) of model 1 shown in Figure 3 illustrates that the unpaired electron is primarily localized within the π^* orbital of the coordinated NO ligand. Thus, provided the {ES-NO}^{7} has a similar electronic configuration, the decreased spin density on the ferrous iron explains why no hyperfine line broadening was resolved in EPR experiments using [^{15}N]-L-cysteine (data not shown).

DISCUSSION

One of the most striking features of the CDO {ES-NO}^{7} complex is the low-spin ferrous iron electronic configuration. Typically, thiols are considered to be relatively weak field ligands, and thus, a thiolate coordination from L-cysteine cannot adequately explain the low-spin configuration of the CDO {ES-NO}^{7} complex. For example, isopenicillin-N-synthase (IPNS) is a member of the 2H1C family of non-heme iron enzymes and catalyzes the O$_2$-dependent ring closure of a tripeptide precursor, δ-(L-α-aminoadipoyl)-L-cysteinyl-D-valine (ACV), to produce the bicyclic isopenicillin-N (*68*−*70*). As with CDO, the ferrous iron active site of IPNS binds ACV via a cysteine thiolate. However, EPR and Mössbauer spectroscopic characterization of the IPNS·ACV·NO complex indicates an {FeNO}^{7} ($S = {}^3/_2$) electronic configuration typical for non-heme mononuclear iron centers (*71*, *72*). Alternatively, the amine group of L-cysteine represents a much stronger field ligand (more so if deprotonated) and thus likely contributes significantly to the ferrous iron d-orbital splitting. Furthermore, the majority of model complexes that exhibit an {FeNO}^{7} ($S = {}^1/_2$) electronic configuration contain an amido-rich first-coordination sphere analogous to that observed for substrate-bound CDO (*63*, *64*, *67*). The microwave power necessary for half-saturation ($P^{1/2} = 1.3$ mW) of the CDO {ES-NO}^{7} signal at 20 K is significantly lower (∼7-fold) than that observed at 8 K for the substrate-bound {FeNO}^{7} ($S = {}^3/_2$) iron−nitrosyl adduct of the 2H1C enzyme, 1-aminocyclopropane-1-carboxylate oxidase (*73*). The slower relaxation observed for the CDO {ES-NO}^{7} ($S = {}^1/_2$) species can largely be attributed to the lower spin state and ligand-centered paramagnetism.

These studies support the first two steps in the proposed mechanism for CDO catalysis. First, CDO stabilizes a resting Fe^{II} state under aerobic conditions in the absence of any additional reductant. Second, this enzyme uses an ordered binding of L-cysteine followed by NO to generate a novel {ES-NO}^{7} ($S = {}^1/_2$) complex. Only trace amounts of an $S = {}^3/_2$ {FeNO}^{7} species are observed during additions of NO to CDO in the absence of substrate. The decreased reactivity of CDO toward NO in the absence of substrate is consistent with the well-established NO and O$_2$ binding behavior exhibited by 2H1C enzymes (*24*−*26*, *69*, *71*, *74*, *75*). Presumably, the bidentate coordination of L-cysteine would decrease the reduction potential of the mononuclear iron active site, resulting in a higher reactivity of the substrate-bound CDO toward both NO and O$_2$.

In the work by Ye et al. (*15*), they observed that the decrease in the enzymatic activity of the Y157F CDO mutant was proportional to the loss of iron incorporation. On the basis of this result, they proposed that one possible role for the C93−Y157 adduct is to stabilize a terminal solvent ligand through hydrogen bonding to protect the ferrous iron site from oxidation (*15*). As illustrated in Scheme 2, in the absence of substrate, the three His residues and the terminal solvent molecule form a nearly tetrahedral geometry at the iron site. Given the short bond distance (<2.2 Å from the iron site; wat4, PDB entry 2B5H; wat160, PDB entry 2ATF) between the bound solvent molecule and the iron site, this terminal ligand is likely a hydroxide ion (*14*, *16*). The presence of an additional hydroxide ion (potentially wat162, PDB entry 2ATF) (*14*) within the active site would effectively neutralize the charge of the monocationic ferrous active site. The hydrogen bond between E104 and H140 results in a unique L-cysteine amine binding site *trans* to H140. Subsequent ligation of the L-cysteine thiol group within the trigonal plane opposite H86 and H88 displaces the terminal solvent molecule and positions the carboxylate group of L-cysteine at a favorable distance for charge stabilization by the R60 guanidinium group. This ternary interaction between L-cysteine and the enzyme active site effectively explains the high substrate specificity demonstrated by CDO. Furthermore, the hydroxide ligand(s) can serve as proton acceptors for both the cysteine thiol and amine functional groups upon substrate coordination. Once the substrate-bound CDO active site is formed, the iron site would be available for NO (and presumably O$_2$) ligation. On the basis of the DFT model of the CDO {ES-NO}^{7} complex shown in Figure 3, the binding of O$_2$ to the iron center of CDO results in a distorted octahedral geometry at the active site. The open coordination site *trans* to H86 is in a relatively hydrophobic pocket and thus provides a reasonable binding site for O$_2$. Moreover, binding at this site would position the bound O$_2$ at a favorable distance (2.2 Å) for initiation of oxidation of C93 to generate the covalent C93−Y157 pair in a catalytic process that is distinct from cysteine oxidation. In the previous X-ray absorption (XAS) spectroscopic work performed by Chai et al. (*65*), an increase in the CDO coordination number was observed

Scheme 2

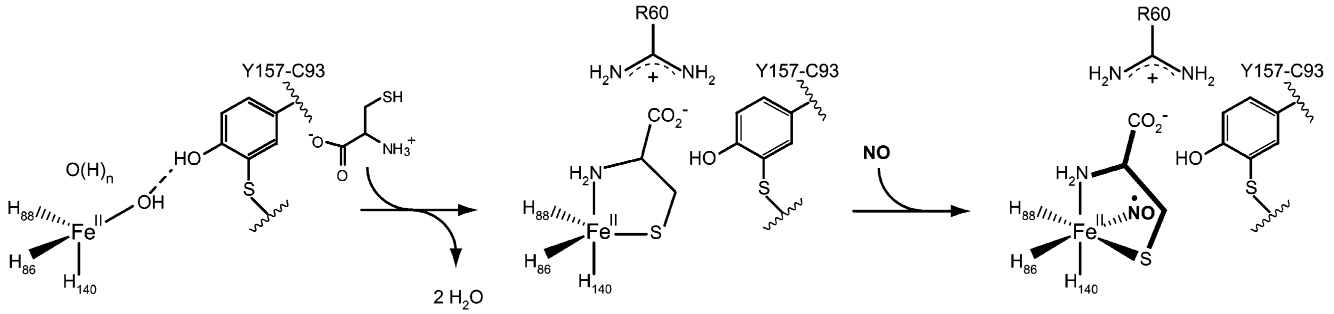

upon addition of L-cysteine. However, the XAS data obtained for substrate-bound CDO exhibited features typical of a O/N coordinating ligand but provided no evidence for coordination of sulfur to the iron center (*13*). This result could imply that the L-cysteine amine group represents the initial coordination point between substrate and ferrous iron and that the thiol coordination may be relatively transient in the absence of NO or O_2. This would also explain the larger *B* factors observed for the iron-coordinated amine and thiol groups of L-cysteine relative to the three His residues in the human substrate-bound CDO crystal structure (*15*).

On the basis of the similarity to the covalently cross-linked Cys−Tyr adduct (C228−Y272) within galactose oxidase (GO), it is reasonable to presume that the mechanism of formation of an analogous pair within CDO (C93−Y157) is similar; that is, this adduct is generated by ferrous iron by an O_2-dependent pathway (*18*, *20*, *76*, *77*). However, unlike the Cu^I metal site within GO, the CDO ferrous iron can readily contribute more than a single electron during enzymatic turnover. Thus, the C93−Y157 adduct is not necessarily required as an additional electron source. Moreover, the complete lack of CDO inhibition in the presence of excess free radical scavenger strongly suggests that a radical-based mechanism similar to that of galactose oxidase is unlikely. Furthermore, no evidence of a stable tyrosine radical in CDO has been observed by either UV−visible or EPR spectroscopy.

In conclusion, the reactivity exhibited by the three-His facial triad motif within CDO parallels many aspects of the 2H1C class of mononuclear non-heme iron enzymes. However, the effect of changing the first coordination sphere from a monoanionic 2H1C to a neutral three-His ligand set may have a profound impact on the reduction potential of the iron center and, thus, the transient intermediates generated during substrate oxidation. Interestingly, in addition to conferring remarkable substrate specificity, the bidentate (amine/thiolate) coordination of L-cysteine to the ferrous iron active site results in the formation of a low-spin $\{FeNO\}^7$ ($S = {}^1/_2$) species more commonly observed in synthetic model complexes and five-coordinate heme metalloenzymes.

ACKNOWLEDGMENT

We acknowledge all members of the University of Wisconsin Center for Structural Genomics (NIH Grant PSI 1U54 GM074901, J. L. Markley, principal investigator, and G. N. Phillips, Jr., and B. G. Fox, co-investigators) for providing the CDO clone. We also thank Michael Hendrich (Carnegie Mellon University) for providing the EPR analysis software (SpinCount) and George Reed (University of Wisconsin) for giving us access to his EPR instrumentation.

REFERENCES

1. Stipanuk, M. H. (2004) Sulfur amino acid metabolism: Pathways for production and removal of homocysteine and cysteine, *Annu. Rev. Nutr. 24*, 539−577.
2. Ewetz, L., and Sorbo, B. (1966) Characteristics of the cysteinesulfinate-forming enzyme system in rat liver, *Biochim. Biophys. Acta 128*, 296−305.
3. Sorbo, B., and Ewetz, L. (1965) The enzymatic oxidation of cysteine to cysteinesulfinate in rat liver, *Biochem. Biophys. Res. Commun. 18*, 359−363.
4. Lombardini, J. B., Singer, T. P., and Boyer, P. D. (1969) Cysteine oxygenase, *J. Biol. Chem. 244*, 1172−1175.
5. Simmons, C. R., Hirschberger, L. L., Machi, M. S., and Stipanuk, M. H. (2006) Expression, purification, and kinetic characterization of recombinant rat cysteine dioxygenase, a non-heme metalloenzyme necessary for regulation of cellular cysteine levels, *Protein Expression Purif. 47*, 74−81.
6. Kwon, Y. H., and Stipanuk, M. H. (2001) Cysteine regulates expression of cysteine dioxygenase and γ-glutamylcysteine synthetase in cultured rat hepatocytes, *Am. J. Physiol. 280*, E804−E815.
7. Cooper, A. J. (1983) Biochemistry of sulfur-containing amino acids, *Annu. Rev. Biochem. 52*, 187−222.
8. Bagley, P. J., Hirschberger, L. L., and Stipanuk, M. H. (1995) Evaluation and modification of an assay procedure for cysteine dioxygenase activity: HPLC method for measurement of cysteine sulfinate and demonstration of physiological relevance of cysteine dioxygenase activity in cysteine catabolism, *Anal. Biochem. 227*, 40−48.
9. Gordon, C., Emery, P., Bradley, H., and Waring, H. (1992) Abnormal sulfur oxidation in systemic lupus erythematosus, *Lancet 229*, 25−26.
10. Heafield, M. T., Fearn, S., Steventon, G. B., Waring, R. H., Williams, A. C., and Sturman, S. G. (1990) Plasma cysteine and sulfate levels in patients with motor neurone, Parkinson's and Alzheimer's disease, *Neurosci. Lett. 110*, 216−220.
11. Slivka, A., and Cohen, G. (1993) Brain ischemia markedly elevates levels of the neurotoxic amino acid, cysteine, *Brain Res. 608*, 33−37.
12. McBean, G. J., and Flynn, J. (2001) Molecular mechanisms of cysteine transport, *Biochem. Soc. Trans. 29*, 717−722.
13. Chai, S. C., Jerkins, A. A., Banik, J. J., Shalev, I., Pinkham, J. L., Uden, P. C., and Maroney, M. J. (2005) Heterologous expression, purification, and characterization of recombinant rat cysteine dioxygenase, *J. Biol. Chem. 280*, 9865−9869.
14. McCoy, J. G., Bailey, L. J., Bitto, E., Bingman, C. A., Aceti, D. J., Fox, B. G., and Phillips, G. N., Jr. (2006) Structure and mechanism of mouse cysteine dioxygenase, *Proc. Natl. Acad. Sci. U.S.A. 103*, 3084−3089.
15. Ye, S., Wu, X. a., Wei, L., Tang, D., Sun, P., Bartlam, M., and Rao, Z. (2007) An insight into the mechanism of human cysteine dioxygenase: Key roles of the thioether-bonded tyrosine cysteine cofactor, *J. Biol. Chem. 282*, 3391−3402.
16. Simmons, C. R., Liu, Q., Huang, Q., Hao, Q., Begley, T. P., Karplus, P. A., and Stipanuk, M. H. (2006) Crystal structure of

mammalian cysteine dioxygenase: A novel mononuclear iron center for cysteine thiol oxidation, *J. Biol. Chem. 281*, 18723−18733.

17. Straganz, G. D., and Nidetzky, B. (2006) Variations of the 2-His-1-carboxylate theme in mononuclear non-heme Fe(II) enzymes, *ChemBioChem 37*, 1536−1548.
18. Whittaker, J. W. (2003) Free Radical Catalysis by Galactose oxidase, *Chem. Rev. 103*, 2347−2363.
19. Whittaker, M. M., and Whittaker, J. W. (1990) A tyrosine-derived free radical in apogalactose oxidase, *J. Biol. Chem. 265*, 9610−9613.
20. Firbank, S. J., Rogers, M. S., Wilmot, C. M., Dooley, D. M., Halcrow, M. A., Knowles, P. F., McPherson, M. J., and Phillips, S. E. V. (2001) From the cover: Crystal structure of the precursor of galactose oxidase: An unusual self-processing enzyme, *Proc. Natl. Acad. Sci. U.S.A. 98*, 12932−12937.
21. Ito, N., Phillips, S. E. V., Stevens, C., Ogel, Z. B., McPherson, M. J., Keen, J. N., Yadav, K. D. S., and Knowles, P. F. (1991) Novel thioether bond revealed by a 1.7 Å crystal structure of galactose oxidase, *Nature 350*, 87−90.
22. Solomon, E. I., Decker, A., and Lehnert, N. (2003) Non-heme iron enzymes: Contrasts to heme catalysis, *Proc. Natl. Acad. Sci. U.S.A. 100*, 3589−3594.
23. Solomon, E. I., Brunold, T. C., Davis, M. I., Kemsley, J. N., Lee, S.-K., Lehnert, N., Neese, F., Skulan, A. J., Yang, Y.-S., and Zhou, J. (2000) Geometric and electronic structure/function correlations in non-heme iron enzymes, *Chem. Rev. 100*, 235−349.
24. Costas, M., Mehn, M. P., Jensen, M. P., and Que, L., Jr. (2004) Diooxygen activation at mononuclear nonheme iron active sites: Enzymes, models, and intermediates, *Chem. Rev. 104*, 939−986.
25. Koehntop, K. D., Emerson, J. P., and Que, L., Jr. (2005) The 2-His-1-carboxylate facial triad: A versatile platform for dioxygen activation by mononuclear non-heme iron(II) enzymes, *J. Biol. Inorg. Chem. 10*, 97−93.
26. Arciero, D. M., and Lipscomb, J. D. (1986) Binding of oxygen-17-labeled substrate and inhibitors to protocatechuate 4,5-dioxygenase-nitrosyl complex. Evidence for direct substrate binding to the active site iron(2+) of extradiol dioxygenases, *J. Biol. Chem. 261*, 2170−2178.
27. Arciero, D. M., Orville, A. M., and Lipscomb, J. D. (1985) [^{17}O]-Water and nitric oxide binding by protocatechuate 4,5-dioxygenase and catechol 2,3-dioxygenase. Evidence for binding of exogenous ligands to the active site iron of extradiol dioxygenases, *J. Biol. Chem. 260*, 14035−14044.
28. Beinert, H., Orme-Johnson, W. H., and Palmer, G. (1978) Special techniques for the preparation of samples for low-temperature EPR spectroscopy, *Methods Enzymol. 54*, 111−132.
29. Sandell, E. B., and Onishi, H. (1978) *Photometric Determination of Traces of Metals: General Aspects*, 4th ed., Wiley, New York.
30. Abragam, A., and Bleaney, B. (1970) *Electron Paramagnetic Resonance of Transition Ions*, International Series of Monographs on Physics, Clarendon, Oxford, U.K.
31. Hendrich, M. P., Petasis, D., Arciero, D. M., and Hooper, A. B. (2001) Correlations of structure and electronic properties from EPR spectroscopy of hydroxylamine oxidoreductase, *J. Am. Chem. Soc. 123*, 2997−3005.
32. Baerends, E. J., Ellis, D. E., and Ros, P. (1973) Self-consistent molecular hartree-fock-slater calculations I. The computational procedure, *Chem. Phys. 2*, 41−51.
33. Guerra, C. F., Snijders, J. G., te Velde, G., and Baerends, E. J. (1998) Towards an order-*N* DFT method, *Theor. Chem. Acc. 99*, 391−403.
34. te Velde, G., and Baerends, E. J. (1992) Numerical integration for polyatomic systems, *J. Comput. Phys. 99*, 84−98.
35. Versluis, L., and Ziegler, T. (1988) The determination of molecular structures by density functional theory. The evaluation of analytical energy gradients by numerical integration, *J. Chem. Phys. 88*, 322−328.
36. Vosko, S. H., Wilk, L., and Nusair, M. (1980) Accurate spin-dependent electron liquid correlation energies for local spin density calculations: A Critical Analysis, *Can. J. Phys. 58*, 1200−1211.
37. Becke, A. D. (1986) Density functional calculations of molecular bond energies, *J. Chem. Phys. 84*, 4524−4529.
38. Perdew, J. P. (1986) Density-functional approximation of the correlation energy of the inhomogeneous electron gas, *Phys. Rev. B 33*, 8822−8824.
39. Berman, H. M., Westbrook, J., Feng, Z., Gilliland, G., Bhat, T. N., Weissig, G., Shindyalov, I. N., and Bourne, P. E. (2000) The Protein Data Bank, *Nucleic Acids Res. 28*, 235−242.
40. Neese, F. (2006) *ORCA: An Ab Initio, Density Functional, and Semiempirical Program Package*, version 2.4, Max Planck Institut für Bioanorganische Chemie, Mülheim an der Ruhr, Germany.
41. Becke, A. D. (1993) A new mixing of hartree-fock and local density-functional theories, *J. Chem. Phys. 98*, 1372−1377.
42. Lee, C., Yang, W., and Parr, R. G. (1988) Development of the Colle-Salvetti correlation-energy formula into a functional of the electron density, *Phys. Rev. B 37*, 785−789.
43. Neese, F. (2002) Prediction and interpretation of the ^{57}Fe isomer shift in Mössbauer spectra by density functional theory, *Inorg. Chim. Acta 337*, 181−192.
44. Wachters, A. J. H. (1970) Gaussian basis set for molecular wavefunctions containing third-row atoms, *J. Chem. Phys. 52*, 1033−1036.
45. Kutzelnigg, W., Fleischer, U., and Schindler, M. (1990) *The IGLO-Method: Ab Initio Calculation and Interpretation of NMR Chemical Shifts and Magnetic Susceptibilities*, Vol. 23, Springer-Verlag, Heidelberg, Germany.
46. Schäfer, A., Horn, H., and Ahlrichs, R. (1992) Fully optimized contracted Gaussian basis sets for atoms Li to Kr, *J. Chem. Phys. 97*, 2571−2577.
47. Eichkorn, K., Treutler, O., Öhm, H., Häser, M., and Ahlrichs, R. (1995) Auxiliary basis sets to approximate Coulomb potentials, *Chem. Phys. Lett. 240*, 283−290.
48. Eichkorn, K., Weigend, F., Treutler, O., and Ahlrichs, R. (1997) Auxiliary basis sets for main row atoms and transition metals and their wse to approximate Coulomb potentials, *Theor. Chem. Acc. 97*, 119−124.
49. Laaksonen, L. (1992) A graphics program for the analysis and display of molecular dynamics trajectories, *J. Mol. Graphics 10*, 33−34.
50. Bergman, D. L., Laaksonen, L., and Laaksonen, A. (1997) Visualization of solvation structures in liquid mixtures, *J. Mol. Graphics Modell. 15*, 301−306.
51. Neese, F. (2001) Prediction of electron paramagnetic resonance *g* values using coupled perturbed Hartree-Fock and Kohn-Sham theory, *J. Chem. Phys. 115*, 11080−11096.
52. Neese, F. (2003) Metal and ligand hyperfine couplings in transition metal complexes: The effect of spin-orbit coupling as studied by coupled perturbed Kohn-Sham theory, *J. Chem. Phys. 118*, 3939−3948.
53. Karlsson, M., Sahlin, M., and Sjöberg, B. M. (1992) *Escherichia coli* ribonucleotide reductase. Radical susceptibility to hydroxyurea is dependent on the regulatory state of the enzyme, *J. Biol. Chem. 267*, 12622−12626.
54. Stubbe, J. (1989) Protein radical involvement in biological catalysis, *Annu. Rev. Biochem. 58*, 257−285.
55. Wanat, A., Schneppensieper, T., Stochel, G., van Eldik, R., Bill, E., and Wieghardt, K. (2002) Kinetics, mechanism, and spectroscopy of the reversible binding of nitric oxide to aquated iron(II). An undergraduate text book reaction revisited, *Inorg. Chem. 41*, 4−10.
56. Schneppensieper, T., Wanat, A., Stochel, G., and van Eldik, R. (2002) Mechanistic information on the reversible binding of NO to selected iron(II) chelates from activation parameters, *Inorg. Chem. 41*, 2565−2573.
57. Dean, J. A. (1992) *Lange's Handbook of Chemistry*, 14th ed., McGraw-Hill, Inc., New York.
58. Hendrich, M. P., Upadhyay, A. K., Riga, J., Arciero, D. M., and Hooper, A. B. (2002) Spectroscopic characterization of the NO adduct of hydroxylamine oxidoreductase, *Biochemistry 41*, 4603−4611.
59. Reginato, N., McCrory, C. T. C., Pervitsky, D., and Li, L. (1999) Synthesis, X-ray crystal structure, and solution behavior of Fe(NO)$_2$(1-MeIm)$_2$: Implications for nitrosyl non-heme-iron complexes with $g = 2.03$, *J. Am. Chem. Soc. 121*, 10217−10218.
60. Lu, S., Libby, E., Saleh, L., Xing, G., Bollinger, J. M. J., and Moenne-Loccoz, P. (2004) Characterization of NO adducts of the diiron center in protein R2 of *Escherichia coli* ribonucleotide reductase and site-directed variants: Implications for the O_2 activation mechanism, *J. Biol. Inorg. Chem. 9*, 818−827.
61. Butler, A. R., and Megson, I. L. (2002) Non-heme iron nitrosyls in biology, *Chem. Rev. 102*, 1155−1165.
62. Bryar, T. R., and Eaton, D. R. (1992) Electronic configuration and structure of paramagnetic iron dinitrosyl complexes, *Can. J. Chem. 70*, 1917−1926.

63. Sellmann, D., Blum, N., Heinemann, F. W., and Hess, B. A. (2001) Synthesis, reactivity, and structure of strictly homologous 18 and 19 valence electron iron nitrosyl complexes, *Chem.—Eur. J. 7*, 1874−1880.
64. Li, M., Bonnet, D., Bill, E., Neese, F., Weyhermèuller, T., Blum, N., Sellmann, D., and Wieghardt, K. (2002) Tuning the electronic structure of octahedral iron complexes [FeL(X)] (L = 1-alkyl-4,7-bis(4-tert-butyl-2-mercaptobenzyl)-1,4,7-triazacyclononane, X = Cl, CH_3O, CN, NO). The S = 1/2 − S = 3/2 spin equilibrium of [FeL^{Pr}(NO)], *Inorg. Chem. 41*, 3444−3456.
65. Chai, S. C., Bruyere, J. R., and Maroney, M. J. (2006) Probes of the catalytic site of cysteine dioxygenase, *J. Biol. Chem. 281*, 15774−15779.
66. Brown, C. A., Pavlosky, M. A., Westre, T. E., Zhang, Y., Hedman, B., Hodgson, K. O., and Solomon, E. I. (1995) Spectroscopic and theoretical description of the electronic structure of S = 3/2 iron-nitrosyl complexes and their relation to O_2 activation by non-heme iron enzyme active sites, *J. Am. Chem. Soc. 117*, 715−732.
67. Serres, R. G., Grapperhaus, C. A., Bothe, E., Bill, E., Weyhermuller, T., Neese, F., and Wieghardt, K. (2004) Structural, spectroscopic, and computational study of an octahedral, non-heme $\{Fe\text{-}NO\}^{6-8}$ series: $[Fe(NO)(cyclam\text{-}ac)]^{2+}$, *J. Am. Chem. Soc. 126*, 5138−5153.
68. Lange, S. J., and Que, L., Jr. (1998) Oxygen activating nonheme iron enzymes, *Curr. Opin. Chem. Biol. 2*, 159−172.
69. Borovok, I., Landman, O., Kreisberg-Zakarin, R., Aharonowitz, Y., and Cohen, G. (1996) Ferrous active site of isopenicillin N synthase: Genetic and sequence analysis of the endogenous ligands, *Biochemistry 35*, 1981−1987.
70. Long, A. J., Clifton, I. J., Roach, P. L., Baldwin, J. E., Rutledge, P. J., and Schofield, C. J. (2005) Structural studies on the reaction of isopenicillin N synthase with the truncated substrate analogues δ-(L-α-aminoadipoyl)-L-cysteinyl-D-α-aminobutyrate, *Biochemistry 44*, 6619−6628.
71. Orville, A. M., Chen, V. J., Kriauciunas, A., Harpel, M. R., Fox, B. G., Munck, E., and Lipscomb, J. D. (1992) Thiolate ligation of the active site iron(II) of isopenicillin N synthase derives from substrate rather than endogenous cysteine: Spectroscopic studies of site-specific Cys−Ser mutated enzymes, *Biochemistry 31*, 4602−4612.
72. Zhang, Y., and Oldfield, E. (2004) On the Mossbauer spectra of isopenicillin N synthase and a model $\{FeNO\}^7$ (S = >3/2) system, *J. Am. Chem. Soc. 126*, 9494−9495.
73. Rocklin, A. M., Tierney, D. L., Kofman, V., Brunhuber, N. M. W., Hoffman, B. M., Christoffersen, R. E., Reich, N. O., Lipscomb, J. D., and Que, L., Jr. (1999) Role of the nonheme Fe(II) center in the biosynthesis of the plant hormone ethylene, *Proc. Natl. Acad. Sci. U.S.A. 96*, 7905−7909.
74. Davis, M. I., Orville, A. M., Neese, F., Zaleski, J. M., Lipscomb, J. D., and Solomon, E. I. (2002) Spectroscopic and electronic structure studies of protocatechuate 3,4-dioxygenase: Nature of tyrosinate-Fe(III) bonds and their contribution to reactivity, *J. Am. Chem. Soc. 124*, 602−614.
75. Que, L., Jr., and Ho, R. Y. N. (1996) Dioxygen activation by enzymes with mononuclear non-heme iron active sites, *Chem. Rev. 96*, 2607−2624.
76. Whittaker, M. M., and Whittaker, J. W. (2003) Cu(I)-dependent biogenesis of the galactose oxidase redox cofactor, *J. Biol. Chem. 278*, 22090−22101.
77. Xie, L., and van der Donk, W. A. (2001) Homemade cofactors: Self-processing in galactose oxidase, *Proc. Natl. Acad. Sci. U.S.A. 98*, 12863−12865.

BI700662D